BNL-229133-2025-JAAM

Tunable broadband luminescence in lead-free hybrid copper halides

Y. Li, M. Cotlet

To be published in "Journal of Energy Chemistry"

October 2025

Center for Functional Nanomaterials

Brookhaven National Laboratory

U.S. Department of Energy

USDOE Office of Science (SC), Basic Energy Sciences (BES). Scientific User Facilities (SUF)

DISCLAIMER

Tunable Broadband Luminescence in Lead-Free Hybrid Copper Halides

Yanyan Li[a,b], Ali Azmy[c], Shunran Li[a,b], Huiju Lee[d], Benjamin T. Diroll[e], Mircea Cotlet[f], Lukasz Wojtas[c], Yi Xia[d], Ido Hadar[g], Ioannis Spanopoulos[c], Peijun Guo[a,b,*]

[a] *Department of Chemical and Environmental Engineering, Yale University, New Haven, CT 06520, USA*
[b] *Energy Sciences Institute, Yale University, West Haven, CT 06516, USA*
[c] *Department of Chemistry, University of South Florida, Tampa, FL33620, USA*
[d] *Department of Mechanical and Materials Engineering, Portland State University, Portland, OR 97201, USA*
[e] *Center for Nanoscale Materials, Argonne National Laboratory, Lemont, IL 60439, USA*
[f] *Center for Functional Nanomaterials, Brookhaven National Laboratory, Upton, NY 11973, USA*
[g] *Institute of Chemistry, and the Center for Nanoscience and Nanotechnology, The Hebrew University of Jerusalem, Jerusalem, 91904, Israel*

[*]Corresponding author.
E-mail address: peijun.guo@yale.edu (P. Guo)

ABSTRACT

Metal halides are an important class of optoelectronic materials combining exceptional optical and electronic properties. An inherent advantage of metal halides is their solution synthesis and processability, which render them as low-cost and environmentally friendly materials for a range of applications from photovoltaics and photodetection to solid-state lighting (SSL). In this study, we synthesized three previously unreported lead-free organic-inorganic hybrid copper halides: $(OA)_4CuX_5$ (X=Br, I; $OA^+=C_8H_{17}NH_3^+$, *n*-octylammonium cation) and $(HA)_2CuI_3$ ($HA^+=C_6H_{13}NH_3^+$, *n*-hexylammonium cation), all of which exhibit broadband emissions arising from self-trapped excitons (STEs). Among these compounds, $(OA)_4CuI_5$ demonstrates tunable dual-band white-light emission with a high color

rendering index value of 91 at room temperature. Temperature-dependent photoluminescence measurements and first-principles calculations reveal distinct behaviors between the two emission states in $(OA)_4CuI_5$. These findings highlight the potential of copper halide compounds for optoelectronic applications, particularly in the development of environmentally friendly solid-state lighting technologies.

Keywords: Lead-free; Solid-state lighting; Copper halides; self-trapped excitons

1. Introduction

White-lighting emitting (WLE) materials have attracted significant attention over the past decades for their potential to provide energy-efficient alternatives to traditional incandescent and fluorescent lamps in solid-state lighting (SSL) applications.[1-4] Single-phase white-light emitters are particularly appealing for next-generation illumination technologies due to their high color rendering index (CRI), good device efficiency, and enhanced stability.[5,6] Low-dimensional organic-inorganic hybrid lead halide perovskites have been extensively studied as WLE materials because of their remarkable photophysical properties and structural versatility.[7-11] However, concerns regarding the toxicity and environmental impact of lead-based WLE materials have prompted efforts to develop lead-free alternatives, which retain the beneficial properties of lead halide perovskites. Lead-free halides offer promising solutions for next-generation SSL technologies.

Among the various lead-free alternatives, copper-based halides are eco-friendly and exhibit desirable optical and structural properties.[12,13] The $3d^{10}$ electronic configuration of copper facilitates diverse coordination numbers, geometries, and bonding modes with halogens, resulting in structural diversity and a wide range of photophysical properties within the copper halide family.[14] Since the discovery of the blue-emissive all-inorganic $Cs_3Cu_2I_5$ single crystals with a high photoluminescence

quantum yield (PLQY) of 90%,[15] copper(I)-based metal halides have emerged as promising candidates for luminescent materials. Subsequent research has led to the development of a variety of high-efficiency luminescent materials based on Cu(I), including $CsCu_2I_3$,[16] $Cs_3Cu_2X_5$ (X=I, Br/I, Br, Br/Cl, Cl),[17-19] Rb_2CuX_3 (X=Cl, Br),[20,21] and K_2CuX_3(X=Cl, Br).[22,23] These materials demonstrate the potential of copper-based halides as versatile and efficient components for next-generation WLE devices.

To enhance the tunability of optical properties, researchers have explored substituting the A-site cation in alkali copper(I) halides with organic cations, leading to hybrid copper halides with greater structural and chemical diversity. These efforts have focused on understanding the relationships between crystal structure and optical properties in emissive hybrid Cu(I) halides. Notable examples include $(MA)_4Cu_2Br_6$ ($MA=CH_3NH_3^+$),[24] $(Gua)_3Cu_2I_5$ (Gua=guanidine),[25] $(PEA)CuI_2$ ($PEA=C_6H_5CH_2CH_2NH_3^+$),[26] and $(TMS)_3Cu_2I_5$ (TMS=trimethylsulfonium).[27] These materials exhibit broadband emissions across the visible spectrum, making them attractive for white-light illumination and potentially display technologies, as the single-material approach for producing white light minimizes light loss and enhances energy efficiency. Additionally, dual-band white-light emissions have been demonstrated in zero-dimensional (0D) copper-based halides, such as $(C_{16}H_{36}N)CuI_2$[28] and $(TPA)_2Cu_2I_4$,[14] adding additional tunability to the CRI and emission characteristics.

In this study, we synthesized three new lead-free organic-inorganic hybrid copper halides: $(OA)_4CuX_5$ (X=Br, I; $OA^+=C_8H_{17}NH_3^+$, *n*-octylammonium cation) and $(HA)_2CuI_3$ ($HA^+ = C_6H_{13}NH_3^+$, *n*-hexylammonium cation), abbreviated as OCB, OCI, and HCI, respectively. $(OA)_4CuBr_5$ and $(HA)_2CuI_3$ exhibit broad yellow-light emission,

while $(OA)_4CuI_5$ shows white-light emission characterized by dual photoluminescence (PL) peaks centered at 493 nm and 616 nm. To investigate their intrinsic photophysical properties of two emission states, we measured their temperature-dependent PL using time-integrated and time-resolved PL spectroscopy. Our findings on these new hybrid copper halides can facilitate the development of WLE materials for SSL applications, support their further performance improvement, and deepen the understanding of their underlying photophysical mechanisms.

2. Experimental

2.1. Materials

Copper (I) bromide (CuBr, 98%, Alfa Aesar), copper (I) iodide (CuI, 98%, Acros), n-octylammonium bromide (> 99%, Greatcell Solar Materials), n-octylammonium iodide (> 99%, Greatcell Solar Materials), n-hexylammonium iodide (Greatcell Solar Materials), hydrobromic acid (HBr, 48%, Sigma-Aldrich), hydroiodic acid (HI, 57%, TCI), hypophosphorous acid solution (50 wt.% in H_2O, Sigma-Aldrich). All materials were used as received without further purification.

2.2. Sample preparation

$(OA)_4CuX_5$ (X=Br, I) and $(HA)_2CuI_3$ single crystals were grown by slowly cooling the solution. $(OA)_4CuBr_5$ was prepared by mixing 0.6 mmol of n-octylammonium bromide and 0.15 mmol of CuBr in a solution of 6 mL HBr and 0.6 mL hypophosphorous acid. The mixture was heated to 100 °C for complete dissolution and then gradually cooled to room temperature at a rate of 5 °C/h. Similarly, for $(OA)_4CuI_5$, 0.4 mmol of n-octylammonium iodide and 0.4 mmol of CuI were dissolved in 3 mL HI and 0.6 mL hypophosphorous acid. For $(HA)_2CuI_3$, 0.3 mmol of n-hexylammonium iodide and 0.3 mmol of CuI were dissolved in 1 mL HI and 0.2 mL hypophosphorous acid. Both solutions followed the same cooling process.

2.3. Characterization

Single-crystal X-ray diffraction (SCXRD) data were measured on Bruker D8 Venture Photon III diffractometer equipped with a Cu Kα INCOATEC ImuS micro-focus source (λ=1.54178 Å). Indexing was performed using APEX4[29] (Difference Vectors method). Data integration and reduction were performed using SaintPlus.[30] Absorption correction was performed by multi-scan method implemented in SADABS.[31] Space group was determined using XPREP implemented in APEX3.[29] The structure was solved using SHELXT[32] and refined using SHELXL-2019/1 (full-matrix least-squares on F2)[33] through OLEX2 interface program.[34] Ellipsoid plot was done with Platon.[35] Powder X-ray diffraction (PXRD) data of single crystals were obtained by using a Rigaku SmartLab X-ray diffractometer with Cu Kα radiative (λ=1.5418 Å). PL and time-resolved PL (TRPL) measurements were conducted by excitation wavelength of 257 nm using a fs Yb:KGW laser (Pharos, Light Conversion) from its four-harmonic generation. PL spectra was captured by a Si EMCCD (Andor iXon Life 888), and time-resolved PL was collected by a streak camera (Hamamatsu C10910 with the Slow sweep unit; M10913). For the temperature-dependent PL and TRPL measurements, samples were mounted in a helium cryostat (DE-204SF, Advanced Research Systems) under vacuum. PL excitation (PLE) measurements of samples were performed by using Horiba Nanolog Fluorescence Spectrometer. The PLQY of our samples was measured using an Edinburgh FLS1000 fluorimeter with an integrating sphere. Raman measurements were performed using a homemade microscope-integrated spectrometer system;[36] the sample was placed in an optical cryostat (Janis VPF-100), which was evacuated to maintain a pressure below 1×10^{-4} Torr. A temperature controller (LakeShore 330) regulated the cryostat temperature, while liquid nitrogen was added to cool the sample down to 77 K. Raman excitation

was provided by a frequency-stabilized 785 nm laser (Toptica). The inelastically scattered Raman signal was directed into a spectrograph (Horiba iHR550, grating 950 grooves/mm) and resolved using a CCD camera (Horiba Syncerity).

3. Results and discussion

Crystals of $(OA)_4CuX_5$ (X = Br, I) are obtained by the reaction of Cu(I) halide salt with n-octylamine in a hot solution of the corresponding hydrohalic acid in the presence of H_3PO_2. Having a closer look at the structure of $(OA)_4CuBr_5$ obtained from XRD analysis (Tables S1-3), it is evident that the structure crystallizes in triclinic space group *P*-1 and consists of isolated $[CuBr_4]^{3-}$ that are separated and charge-balanced by four octyl-ammonium counter cations and one discreet Br^- anion. Each $[CuBr_4]^{3-}$ tetrahedron features an average bond length of 2.4855 Å, a Δd value of 0.01674 and a σ^2 of 30 deg^2 (Fig. 1a,b) which are consistent with other reported hybrid Cu(I) bromides such as $(AEP)_2Cu_2Br_6{\cdot}2Br{\cdot}2H_2O$ (AEP = $C_6H_{18}N_{33}^+$).[37] A comparison of the experimental PXRD pattern of the main phase of $(OA)_4CuBr_5$ against the calculated pattern from the crystal structure from XRD analysis is presented in Fig. 2a, validating phase purity.

Interestingly, during crystallization of $(OA)_4CuBr_5$ a secondary phase with the same formula and structure was identified based on XRD studies. Despite multiple attempts to finalize the structure, due to crystal quality, this was impossible. However, we showcase corresponding unit cell parameters and crystal structure in Table S4 and Fig. S1. Comparing the two compounds, we observe a significant difference in the organic part configuration, which is less distorted in the main phase, while the corresponding unit cell volume of the impurity phase is larger for the secondary phase as compared to the main phase (2276 versus 2490 $Å^3$ respectively).

Although the as-made $(OA)_4CuI_5$ crystals looked uniform and well-faceted, attempts to solve the single crystal structure using XRD studies were impossible due to

crystal quality. Therefore, unit cell parameters were identified by the Powley fitting of the experimental PXRD data, which, surprisingly, match pretty well with the secondary phase of $(OA)_4CuBr_5$ (Table S5, Fig. S2a). Fig. 2b shows a comparison between the experimental PXRD pattern of $(OA)_4CuI_5$ against the calculated PXRD pattern obtained from the crystal structure of $(OA)_4CuBr_5$ secondary phase, validating the claim that these compounds are isostructural. To further verify this hypothesis, we calculated the corresponding d-spacing for each crystal plane based on the position of the Bragg peaks of the two sets of diffractions. As shown in Fig. S2b, this linear relationship of the d-spacing between $(OA)_4CuBr_5$ (d_1) and $(OA)_4CuI_5$ (d_2) strongly supports this assumption.

Similarly, upon the reaction of CuI with n-hexylammonium iodide in hot HI solution in the presence of H_3PO_2, colorless plate crystals of $(HA)_2CuI_3$ are acquired. Single crystal X-ray diffraction (XRD) studies demonstrate that the structure crystallizes in the centrosymmetric monoclinic space group *C*2/*c* with 0D $[Cu_2I_6]^{4-}$ dimers separated and charge-balanced by hexylammonium molecules. Each $[Cu_2I_6]^{4-}$ dimer consists of two edge-sharing $[CuI_4]^{2-}$ tetrahedra derived from one copper atom and three crystallographically independent iodide atoms with average Cu-I bond lengths of 2.6656 Å, which is comparable to Cu(I)-I bond lengths of other reported 0D copper halides (Fig. 1c,d).[27,28] These face-sharing octahedra feature a bond length distortion (Δd), $\Delta d = \frac{1}{4}\sum_{i=1}^{4}(\frac{d_i - d_0}{d_i})^2$, ($d_i$ are the four Cu-I bond lengths and d_0 is the mean Cu-I bond length within the tetrahedron) of 0.01772, and a bond angle variance (σ^2), $\sigma^2 = \frac{1}{5}\sum_{i=1}^{6}(\theta_i - 109.47)^2$ (where θ_i are the six I-Cu-I bond angles within the tetrahedron) of 48 deg^2.[38,39] The corresponding notable tetrahedral distortion is ascribed to the presence of multiple hydrogen bonds among the hexylammonium cations and iodide atoms of the metal cluster (Fig. 1d). Powder X-ray diffraction (PXRD) analysis validates the phase purity of the synthesized material since the

experimental PXRD pattern matches its corresponding calculated diffraction pattern from the single crystal structure (Fig. 2c). In addition, $(OA)_4CuBr_5$ exhibits excellent air stability, as confirmed by PXRD measurements showing no changes after one month of ambient storage (Fig. S3).

Density functional theory (DFT) calculations were conducted to investigate the electronic properties of $(OA)_4CuBr_5$ and $(OA)_4CuI_5$ (Fig. S4). Both compounds exhibit a direct bandgap at their Γ point, with calculated values of 2.67 eV and 2.86 eV, respectively. We then conducted X-ray photoemission spectroscopy (XPS) measurements on these three copper-based compounds to measure the valence state of copper. As presented in Fig. S5, the measured binding energies of these compounds are approximately 929.5 and 949.5 eV, which represent the Cu $2p_{3/2}$ and Cu $2p_{1/2}$ and indicate the dominant presence of Cu^+.[40] Moreover, the characteristic satellite peak of Cu^{2+} at ~943 eV was negligible in all these compounds, excluding the divalent Cu^{2+} as impurities in the crystal.[41,42] This finding suggests that Cu^+ remains unoxidized during the bulk crystal growth process.

Variations in crystal structure, cationic ligand steric effects, halide composition, and halogen electronegativity collectively give rise to the distinct emission properties of these hybrid copper halides. Under 257 nm excitation, $(OA)_4CuBr_5$ emits yellow light, with a photoluminescence (PL) peak at 587 nm and a broad full width at half-maximum (fwhm) of approximately 107 nm (Fig. 3a). Its PL excitation (PLE) spectrum shows an absorption peak at 285 nm. Similarly, $(HA)_2CuI_3$ displays broadband yellow luminescence with PL and PLE maxima at 573 and 296 nm, respectively. $(OA)_4CuI_5$ exhibits dual-band white-light emission across the visible region (400-800 nm), with PL peaks at 493 and 616 nm. These emission variations demonstrate the tunable optical properties achieved through adjustment in both the organic cation and halide anion.

Benefiting from the dual-emission of the $(OA)_4CuI_5$ in the blue and yellow region, the Commission Internationale de l'Eclairage (CIE)[43] chromaticity coordinate was calculated to be (0.38, 0.38), positioning it at a warm-white point (Fig. S6). In addition, the color rendering index (CRI) of $(OA)_4CuI_5$, which is defined as the accuracy of a light source to reproduce the standard light source, is determined to be 91, indicating an excellent potential for lighting applications. This value is comparable to that of $(TEA)_2Cu_2Br_2Cl_2$ (95) [44] and significantly higher than that of $(C_{16}H_{36}N)CuI_2$ of (78).[28] Notably, when varying the monitoring wavelength, the PLE spectra (Fig. S7, 8) of $(OA)_4CuBr_5$ and $(HA)_2CuI_3$ maintain a consistent shape, exhibiting only changes in absolute intensity. This behavior indicates the presence of a single excited state in the system. In contrast, for $(OA)_4CuI_5$, when monitoring PL at 493 nm and 616 nm, a dominant PLE peak appears at 290 nm, but a small shoulder emerges at 330 nm (Fig. S9). This dual-emission and dual-excitation behavior suggests the presence of two distinct excited states within the material, both of which contribute to light emission.

Time-resolved PL (TRPL) measurements were carried out to further study their photophysical properties (Fig. 3b, S10). The PL lifetimes were fitted using biexponential fitting. At room temperature, the average lifetimes of $(OA)_4CuI_5$ and $(HA)_2CuI_3$ are 42.7 ns and 41.5 ns, respectively, while $(OA)_4CuBr_5$ exhibits a significantly longer lifetime of 12.2 μs (Table 1). Compared to the short PL lifetimes and narrow bandwidth of free-exciton emission in low-dimensional semiconductors such as $CsPbBr_3$ quantum dots, [47] Cu-based compounds generally exhibit longer PL lifetimes and broader emission spectra, a characteristic widely attributed to self-trapped exciton (STE) emission. [47] Fundamentally, although the wavefunctions of the ground and excited states of carriers in these low-dimensional Cu compounds exhibit significant overlap due to strong quantum confinement, the radiative recombination of

STEs is likely spin-inhibited due to their triplet-state nature. However, spin-orbit coupling, facilitated by the presence of heavy atoms, can mitigate this limitation, enabling the radiative recombination. This is in line with our observation that replacing I^- with Br^- significantly extends the PL lifetime by hundreds of times. However, compared to the ~1 μs lifetimes observed in all-inorganic emissive Cu–I materials (e.g., $Cs_3Cu_2I_5$ and $CsCu_2I_3$),[15,16] the lifetimes of $(HA)_2CuI_3$ and $(OA)_4CuI_5$ are notably shorter. This is unexpected, as replacing Cs^+ with organic cations should weaken the spin-orbit coupling, which would typically lead to a longer lifetime. We propose that this unexpectedly short PL lifetime is influenced by non-radiative recombination because the PL quantum yield (PLQY) of the three compounds discussed in this study are generally low, approximately 0.2% at room temperature, far below that of the reported white-emissive $TPA_2Cu_2I_4$ with PLQY of 94.27%.[14, 46] This suggests that the majority of excitons return to the ground state via non-radiative recombination processes, significantly influencing the observed PL lifetime.

We performed temperature-dependent PL decay experiments to further solidify our assumption. The experimental PL lifetime has the following relationship with the radiative recombination rate and the non-radiative recombination rate:

$$\frac{1}{\tau_{\mathrm{exp}}} = k_{\mathrm{exp}} = k_{\mathrm{rad}} + k_{\mathrm{non-rad}}$$

where τ_{exp} is the experimentally observed PL lifetime, k_{rad} is the radiative recombination rate, and $k_{\mathrm{non-rad}}$ is the non-radiative recombination rate. k_{rad} is an intrinsic property of the material and remains largely independent of temperature. In contrast, $k_{\mathrm{non-rad}}$ is generally highly temperature-dependent and tends to be significantly suppressed at lower temperatures. As shown in Fig. 4, as the temperature decreases from room temperature to 7 K, the PL lifetime initially exhibits a rapid

increase when non-radiative recombination dominates the recombination. Subsequently, the lifetime saturates, accompanied by significant increase in the PL intensity, when the radiative recombination becomes the primary recombination pathway, at which point the experimentally measured PL lifetime reflects the intrinsic lifetime of the material. We determined that the intrinsic PL lifetimes of $(OA)_4CuI_5$ and $(HA)_2CuI_3$ are 3.4 and 2.3 μs (Tables S9-11), respectively, both longer than the ~1 μs lifetime of $Cs_3Cu_2I_5$ and $CsCu_2I_3$. This trend aligns with our earlier conclusions regarding the influence of spin-orbit coupling, where weaker coupling leads to longer lifetimes. In addition to the temperature-dependent PL lifetime, we systematically investigated the effect of temperature on the lineshape of PL spectra. As shown in Fig. 4, the PL peak positions remain nearly unchanged as the temperature decreases, indicating that the energy band structure of these materials is temperature-independent. The primary temperature-dependent trend observed in all three compounds is a narrowing of the emission bandwidth. This can be attributed to the reduction in thermal energy at lower temperatures, which suppresses the population of higher vibrational states. Consequently, the distribution of energy levels involved in the electronic transitions becomes narrower, leading to a more confined PL spectrum. The slight red shift in the PL spectrum of $(OA)_4CuBr_5$ at low temperatures likely arises from lattice relaxation enhanced by weaker exciton–phonon coupling, whereas the more rigid lattices of the other compounds keep their PL peaks stable. Unlike $(OA)_4CuBr_5$, which exhibits only a single STE, $(OA)_4CuI_5$ displays two distinct STE states. This difference is likely due to variations in their local coordination environments and the degree of orbital

hybridization. As shown in the projected density of states (DOS) results (Figure S4c,d), the valence band maximum (VBM) of both OCB and OCI is primarily derived from Cu and halogen orbitals, while the conduction band minimum (CBM) mainly originates from ligand orbitals. This suggests that the emission arises from a combination of metal-to-ligand charge transfer (MLCT) and halide-to-ligand charge transfer (XLCT).[48] Notably, in OCI, the DOS reveals stronger hybridization between Cu-d and I-p orbitals at the VBM, along with enhanced coupling to ligand orbitals at the CBM. The heavier iodine anion further contributes significant spin–orbit coupling, resulting in broader orbital mixing. These features collectively account for the broader and dual-peak white-light emission observed in $(OA)_4CuI_5$. Moreover, the dual-emission characteristic of $(OA)_4CuI_5$ gradually transitions to a single-emission state at low temperatures (Fig. 4e). In the following sections, we will focus on the PL mechanism of $(OA)_4CuI_5$.

As previously discussed, $(OA)_4CuI_5$ exhibits two distinct excited states. Here, we designate the excited state corresponding to the PL peak at 493 nm as ES1, and that associated with the PL peak at 613 nm as ES2. By comparing the PL lifetimes of ES1 and ES2, we observe that both lifetimes increase as the temperature decreases (Fig. 4b, S11, and Table S10). Notably, this trend is more pronounced for ES1 comparing to ES2, indicating that non-radiative recombination is more effectively suppressed at low temperatures for ES1. However, despite this extended lifetime and the predicted enhancement in PL radiative efficiency, the relative intensity of ES1 rapidly diminishes. We attribute this apparent contradiction to the freezing of intersystem transitions between ES1 and ES2 at low temperatures, which alters the population dynamics of the excited states and suppresses the emission from ES1. We use the configuration

coordinate diagram to describe such a temperature-dependent behavior. As shown in Fig. 5a, at higher temperatures, the 257 nm excitation laser initially excites the carriers from the ground state to ES2, followed by rapid relaxation to the thermal equilibrium state of ES2. Subsequently, the excited carriers in ES2 can overcome the energy barrier between ES1 and ES2 via thermal fluctuations at room temperature ($E = k_BT$), enabling intersystem crossing and resulting in the observed dual-emission at room temperature. However, as the temperature decreases and the thermal energy becomes significantly smaller than the energy barrier, intersystem crossing is strongly suppressed, leading to the disappearance of ES1 emission at low temperatures (Fig. 5b). In this scenario, the energy barrier corresponds to the difference between the lowest energy of ES2 and the energy at the intersection of ES1 and ES2, which can be determined by fitting the temperature-dependent ratio of ES2 to ES1(Fig. 5c, S12), using the following equation:[14]

$$\frac{I_{ES2}}{I_{ES1}} = Ae^{\Delta E/\kappa_B T}$$

The fitted *ΔE* is 41.02 meV which is comparable to the thermal energy at room temperature (26 meV). Such energy barrier allows efficient intersystem crossing at room temperature, facilitating the observed dual-emission behavior. Furthermore, the Huang–Rhys factor (*S*) was obtained by fitting the temperature-dependent FWHM using the following equation:[14]

$$FWHM = 2.36\sqrt{S}\hbar\omega_{phonon}\sqrt{coth\frac{\hbar\omega_{phonon}}{2k_BT}}$$

where *ħ* is the reduced Planck constant, ω is the phonon frequency, T is the temperature, and k_B is the Boltzmann constant. The extracted S values for the ES1 and ES2 emissions are 13.36 and 40.78, respectively (Figure S13). These large S values indicate

strong electron–phonon coupling and a soft crystal lattice in $(OA)_4CuI_5$, which facilitates the formation of STEs.

To further investigate this intersystem crossing, we measured the PL spectra of $(OA)_4CuI_5$ using 330 nm excitation (Fig. 6a,b), which corresponds to the optimal excitation of ES1, as identified in previous PLE results (shown in Fig. S9). Specifically, the room-temperature PL spectra under the two different excitations are remarkably similar, both exhibiting a weaker ES1 emission and a stronger ES2 emission. As illustrated in Fig. 6c (defined as stage 1), the energy barrier between ES1 and ES2 is not significantly larger than the thermal energy. Consequently, regardless of whether the carriers are directly excited to ES1 or ES2, rapid thermalization leads to similar carrier population distributions, resulting in nearly identical PL spectra. Interestingly, as temperature decreases slightly (defined as stage 2), the PL intensity of ES1 drops rapidly, resulting in a single emission from ES2, even when ES1 is directly excited. We attribute this phenomenon to a small asymmetry in the energy barriers governing intersystem crossing in opposite directions. We assume that the lowest energy of ES1 is slightly higher than that of ES2 by an energy difference E_0. If we define the energy barrier for the transition from ES1 to ES2 as E_{12}, and the reverse transition from ES2 to ES1 as E_{21}, then the relationship follows:

$$E_{12} + E_0 = E_{21} = 41\ \text{meV}$$

At intermediate temperatures, the thermal energy remains sufficient to facilitate the transition from ES1 to ES2, while the reverse transition from ES2 to ES1 becomes increasingly suppressed. As a result, carriers initially excited to ES1 rapidly relax to ES2, leading to a dominant single-emission feature from ES2 (Fig. 6d). As the temperature decreases further, the thermal energy becomes insufficient to sustain any intersystem crossing, freezing the transitions between ES1 and ES2. At this stage, the

PL spectra are solely determined by the initial population of the excited states upon excitation. This explains why the PL intensity of ES1, after initially disappearing due to preferential relaxation into ES2, eventually re-emerges (stage 3, Fig. 6e).

It is important to note that in the 330 nm-excited PL experiments, ES2 emission persists even when all intersystem crossing is frozen, which appears to contradict our previous analysis. However, this can be explained by the fact that the 330 nm laser can still directly excite ES2, as evidenced by the extended tail of ES2 in the PLE spectra (Fig. 3a). As the temperature decreases further (stage 4), the emissions from ES1 and ES2 diminish, while a new emission peak emerges near 400 nm. We attribute this peak to free exciton emission. It is well-known that the formation of STEs is closely related to lattice rigidity. We propose that the enhancement of FE emission at low temperatures occurs because the lattice becomes more rigid, thereby reducing the propensity for exciton self-trapping and weakening STE formation. We compared the Raman spectra (Fig. S14) of $(OA)_4CuI_5$ at room temperature and 78 K and observed that the Raman peaks shift to higher wavenumbers at 78 K. This shift indicates an increase in lattice rigidity, supporting our hypothesis that the enhanced FE emission at stage 4 results from a suppression of self-trapped exciton formation due to a more rigid lattice. Overall, while dual-emission from ES1 and ES2 is observed in both stage 1 (high-temperature regime) and stage 3 (low-temperature regime), the underlying mechanisms differ. In stage 1, dual emission primarily results from thermalized population redistribution following intersystem crossing. In contrast, in stage 3, where intersystem crossing is frozen, dual emission arises from the comparable excitation efficiency of the 330 nm laser for both ES1 and ES2.

4. Conclusions

In summary, three different organic-inorganic hybrid copper halides were

synthesized. $(OA)_4CuBr_5$ and $(HA)_2CuI_3$ emit broad yellow light with PL peaks at 587 and 573 nm, respectively. Notably, $(OA)_4CuI_5$ exhibits white-light emission with two PL peaks at 493 and 616 nm. All three compounds exhibit large Stokes shifts, broad emission and long intrinsic PL lifetimes, consistent with the characteristics of STE emission previously reported in copper halides. Temperature-dependent PL experiments reveal that the emission properties of $(HA)_2CuI_3$ and $(OA)_4CuBr_5$ remain largely unaffected by temperature variations. In contrast, the PL behavior of $(OA)_4CuI_5$ exhibits strong temperature and excitation wavelength dependence, which is attributed to the presence of two distinct excited states. Our work systematically elucidates the intricate PL dynamics of dual-excited state systems, offering valuable insights into their emission mechanisms. This study serves as a significant reference for future research on dual-emission materials, aiding in the design and optimization of materials with tailored optical properties.

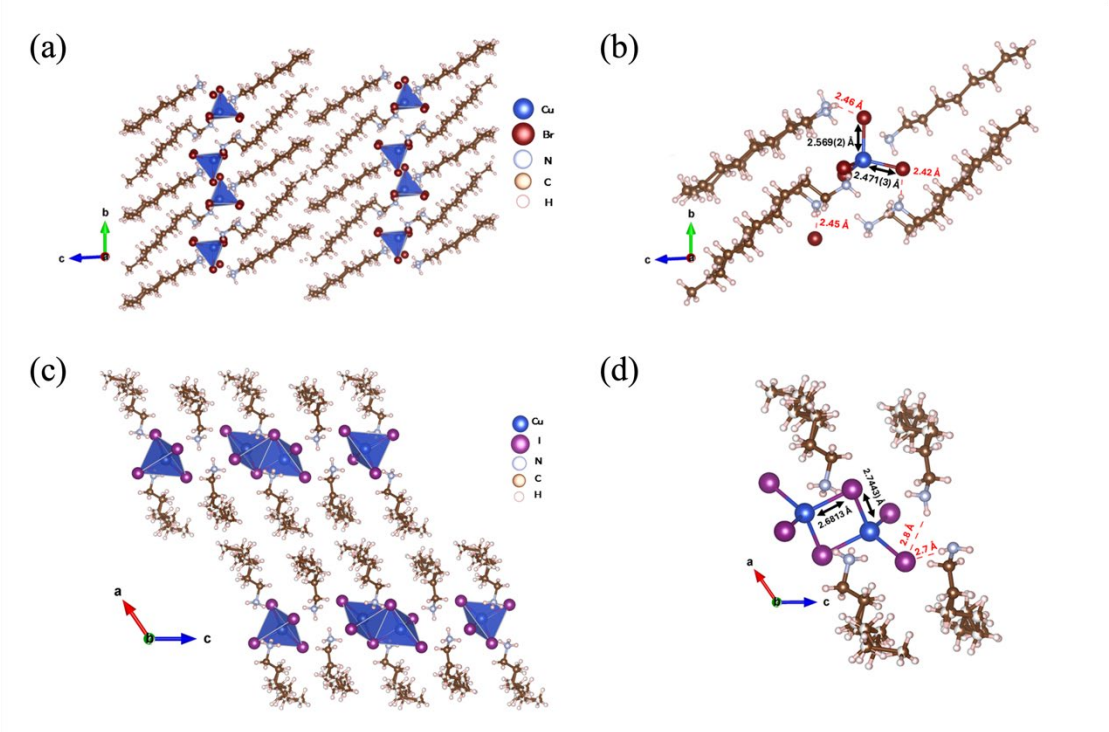

Fig. 1. (a) Crystal structure of $(OA)_4CuBr_5$ as viewed along the *a*-axis. (b) Part of the crystal structure of $(OA)_4CuBr_5$ showing two representative Cu-Br bond lengths and hydrogen bonds among the hydrogen atoms of the ammonium functional groups and the bromide atoms responsible for the $[CuBr_4]^{3-}$ tetrahedral distortion. (c) Crystal structure of $(HA)_2CuI_3$ as viewed along the *b*-axis. (d) Part of the crystal structure of $(HA)_2CuI_3$ showing the inorganic cluster along with two representative Cu-I bond lengths and hydrogen bonds among the hydrogen atoms of the ammonium functional groups and the iodide atoms of the $[Cu_2I_6]^{4-}$ dimers.

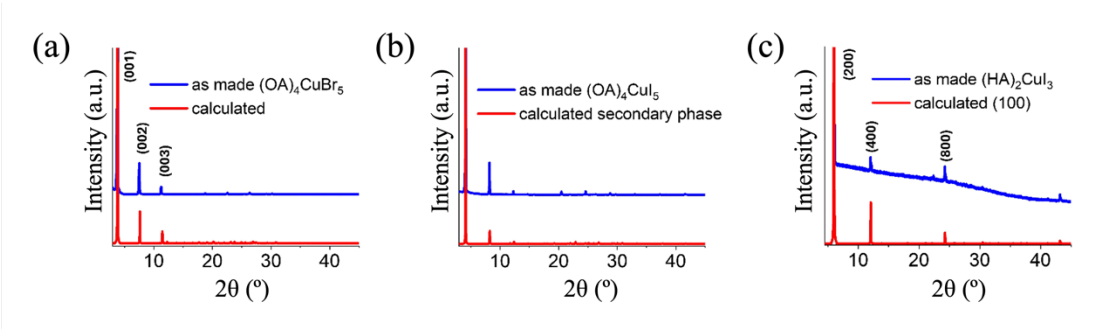

Fig. 2. (a) Comparison of the PXRD patterns of as made $(OA)_4CuBr_5$ to the calculated pattern based on the solved single crystal structure, and (b) comparison of the PXRD patterns of as made $(OA)_4CuI_5$ to the calculated pattern based on the solved single crystal structure of the $(OA)_4CuBr_5$ secondary phase. (c) Comparison of the PXRD patterns of as made $(HA)_2CuI_3$ to the calculated pattern based on the solved single crystal structure including preferred orientation (100).

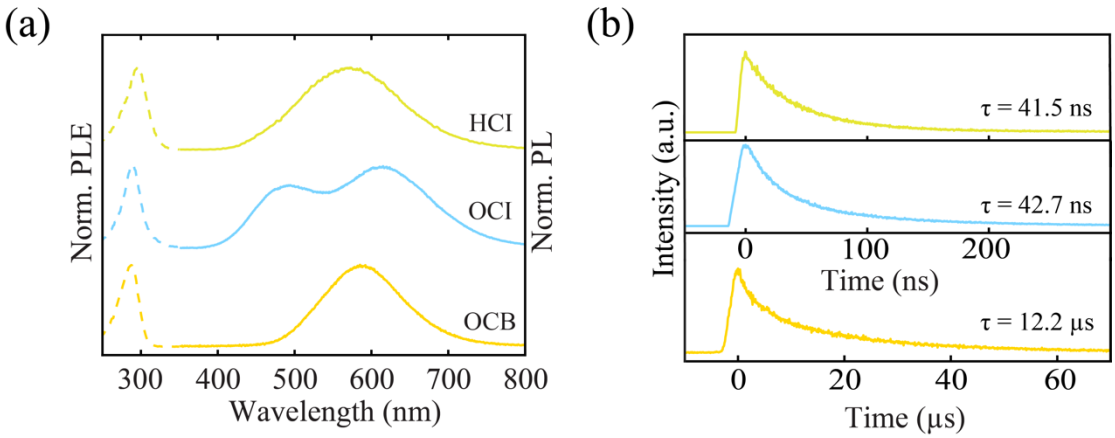

Fig. 3. (a) Normalized PLE and PL spectra of the corresponding bulk crystals measured at room temperature. (b) TRPL spectra of these bulk crystals measured at room temperature. From bottom top are $(OA)_4CuBr_5$, $(OA)_4CuI_5$, and $(HA)_2CuI_3$.

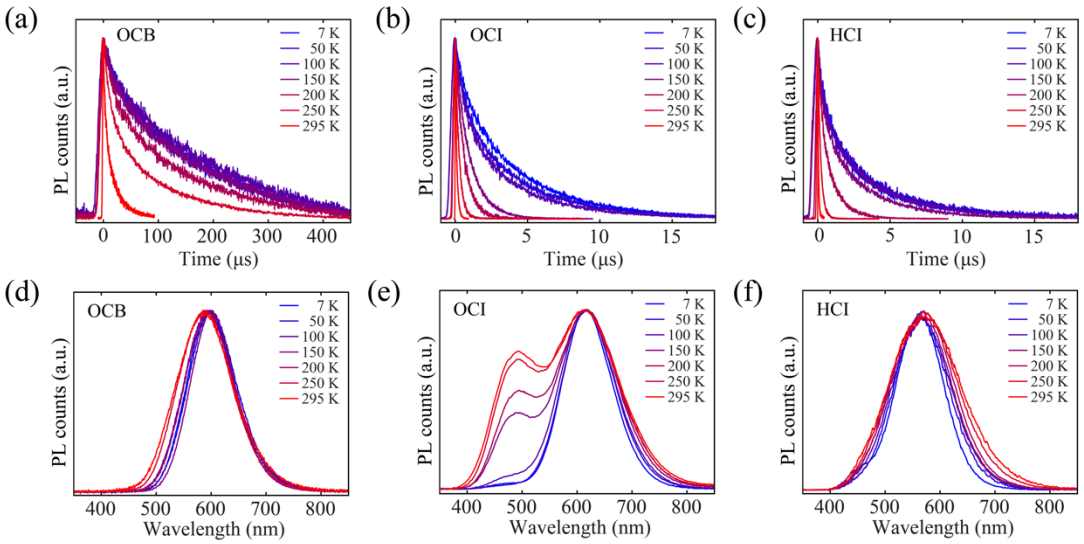

Fig. 4. Temperature-dependent TRPL spectra of (a) $(OA)_4CuBr_5$, (b) $(OA)_4CuI_5$ (extracted at 616 nm), and (c) $(HA)_2CuI_3$, measured from 7 to 295 K (excited at 257 nm). Temperature-dependent PL spectra of (d) $(OA)_4CuBr_5$, (e) $(OA)_4CuI_5$, and (f) $(HA)_2CuI_3$, measured from 7 to 295 K (excited at 257 nm).

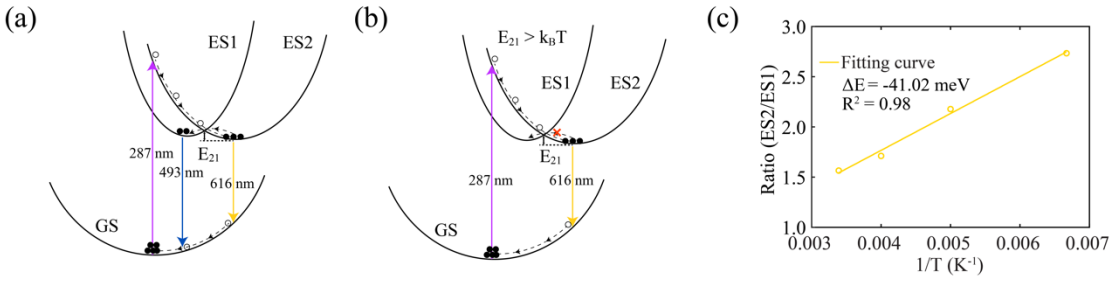

Fig. 5. Configuration coordinate diagrams of intersystem transitions between ES1 and ES2 at (a) higher and (b) lower temperature excited at 257 nm. c) The PL intensity ratio of ES2/ES1 as a function of inverse temperature.

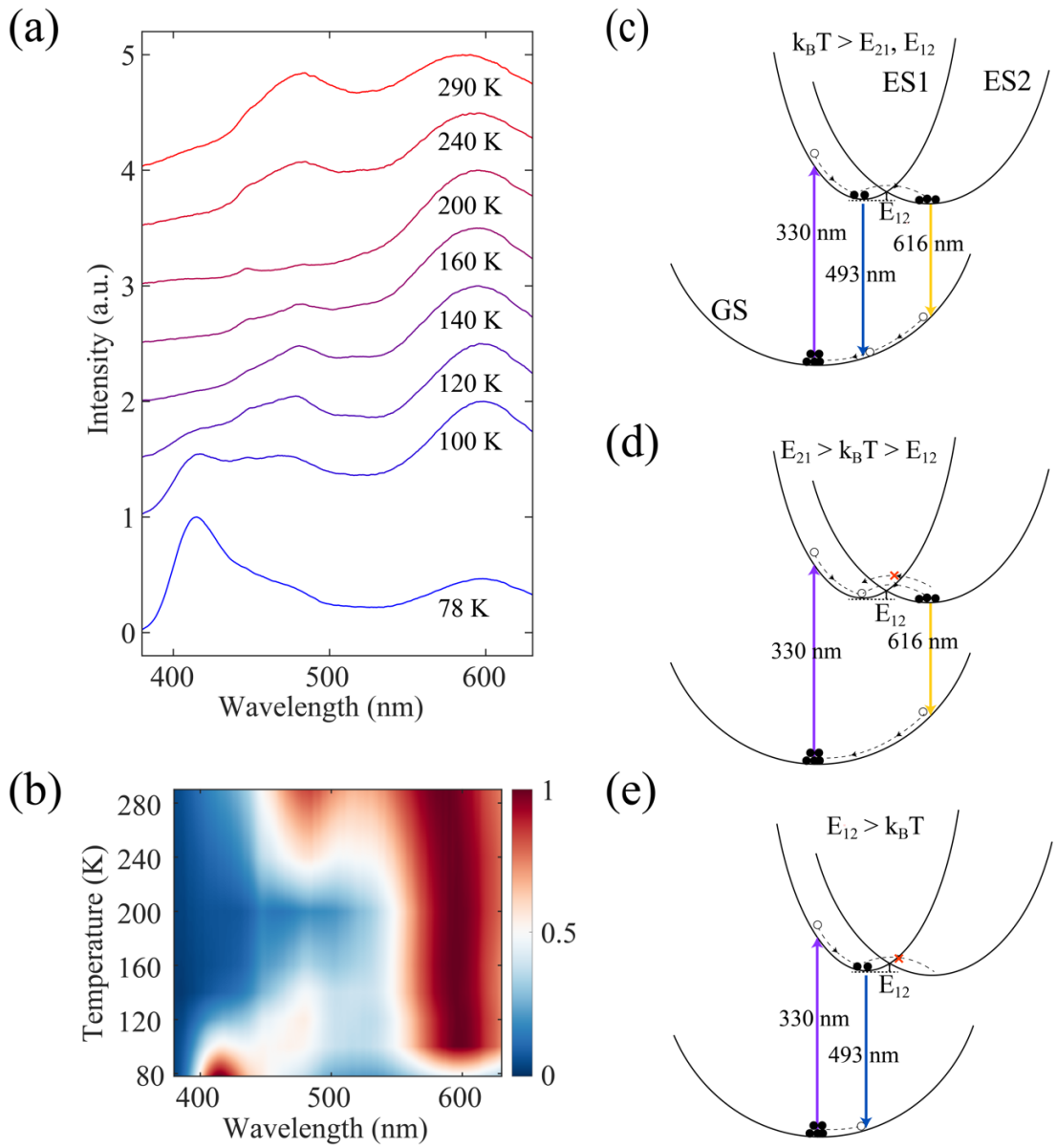

Fig. 6. Temperature-dependent (a) PL spectra and (b) mapping of $(OA)_4CuI_5$ excited at 330 nm. Configuration coordinate diagrams of intersystem transitions between ES1 and ES2 excited at 330 nm at (a) stage 1 (high-temperature regime), (b) stage 2 (intermediate-temperature regime), and (c) stage 3 (low-temperature regime).

Table 1. Summary of optical parameters of three copper-based hybrid compounds.

Compounds	PL peak (nm)	PLE peak (nm)	CIE coordinates	Lifetime
$(OA)_4CuBr_5$	587	285	(0.48, 0.49)	τ_{avg} = 12.2 μs
$(OA)_4CuI_5$	493, 616	290	(0.38, 0.38)	τ_{avg} = 42.7 ns
$(HA)_2CuI_3$	573	296	(0.41, 0.47)	τ_{avg} = 41.5 ns

References

[1] S. Pimputkar, J. S. Speck, S. P. DenBaars and S. Nakamura, Nat. Photonics. 3 (2009) 180-182.

[2] J. Chen, J. Wang, X. Xu, J. Li, J. Song, S. Lan, S. Liu, B. Cai, B. Han and J. T. Precht, Nat. Photonics. 15 (2021) 238-244.

[3] D. Cortecchia, J. Yin, A. Petrozza and C. Soci, J.of Mater. Chem. C. 7 (2019) 4956-4969.

[4] L. Mao, P. Guo, M. Kepenekian, I. Hadar, C. Katan, J. Even, R. D. Schaller, C. C. Stoumpos and M. G. Kanatzidis, J. Am. Chem. Soc. 140 (2018) 13078-13088.

[5] H. Peng, Y. Tian, X. Wang, T. Huang, Z. Yu, Y. Zhao, T. Dong, J. Wang and B. Zou, ACS Appl. Mater. Interfaces. 14 (2022) 12395-12403.

[6] G. Yu, F. Lin, K. Zhou, S. Fang, Y. Shi, W. Liu, H. Hu, B. Ma and H. Lin, Chem. Mater. 33 (2021) 5668-5674.

[7] M. D. Smith and H. I. Karunadasa, Acc. Chem. Res. 51 (2018) 619-627.

[8] G. Zhou, M. Li, J. Zhao, M. S. Molokeev and Z. Xia, Adv. Opt. Mater. 7 (2019) 1901335.

[9] D. Li, W. Wu, S. Wang, X. Zhang, L. Li, Y. Yao, Y. Peng and J. Luo, J. Mater. Chem. C. 8 (2020) 6710-6714.

[10] H. Liu, T. B. Shonde, O. J. Olasupo, T. F. Manny, M. S. Islam, J. Viera, M. Khizr, S. Moslemi, X. Lin and J. R. V. Winfred, Adv. Mater. (2024) 2412239.

[11] E. J. Crace, A. C. Su and H. I. Karunadasa, Chem. Sci. 13 (2022) 9973-9979.

[12] D. Banerjee and B. Saparov, Chem. Mater. 35 (2023) 3364-3385.

[13] Y. Li, Z. Zhou, N. Tewari, M. Ng, P. Geng, D. Chen, P. K. Ko, M. Qammar, L. Guo and J. E. Halpert, Mater. Chem. Front. 5 (2021) 4796-4820.

[14] H. Lv, W. Shao, H. Chen, G. Zhu, Y. Wang, Z. Zhang and H. Liang, Adv. Sci. (2024) 2405995.

[15] T. Jun, K. Sim, S. Iimura, M. Sasase, H. Kamioka, J. Kim and H. Hosono, Adv. Mater. 30 (2018) 1804547.

[16] R. Lin, Q. Guo, Q. Zhu, Y. Zhu, W. Zheng and F. Huang, Adv. Mater. 31 (2019) 1905079.

[17] Y. Li, P. Vashishtha, Z. Zhou, Z. Li, S. B. Shivarudraiah, C. Ma, J. Liu, K. S. Wong, H. Su and J. E. Halpert, Chem. Mater. 32 (2020) 5515-5524.
[18] Z. Luo, Q. Li, L. Zhang, X. Wu, L. Tan, C. Zou, Y. Liu and Z. Quan, Small 16 (2020) 1905226.
[19] L. Lian, M. Zheng, P. Zhang, Z. Zheng, K. Du, W. Lei, J. Gao, G. Niu, D. Zhang and T. Zhai, Chem. Mater. 32 (2020) 3462-3468.
[20] T. D. Creason, A. Yangui, R. Roccanova, A. Strom, M. H. Du and B. Saparov, Adv. Opt. Mater. 8 (2020) 1901338.
[21] A. Kumar, P. Kumar, A. Saini, M. Bag and P. Kar, Small 21 (2025) 2406048.
[22] T. D. Creason, T. M. McWhorter, Z. Bell, M.-H. Du and B. Saparov, Chem. Mater. 32 (2020) 6197-6205.
[23] Z. Zhou, Y. Li, Z. Xing, Z. Li, K. S. Wong and J. E. Halpert, ACS Appl. Nano Mater. 4 (2021) 14188-14196.
[24] H. Peng, S. Yao, Y. Guo, R. Zhi, X. Wang, F. Ge, Y. Tian, J. Wang and B. Zou, J. Phys. Chem. Lett. 11 (2020) 4703-4710.
[25] H. Peng, X. Wang, Y. Tian, B. Zou, F. Yang, T. Huang, C. Peng, S. Yao, Z. Yu and Q. Yao, ACS Appl. Mater. Interfaces. 31 (2021) 13443-13451.
[26] C. Wang, X. Mao, Z. Wang, X. Xu, W. Guo and R. Zhang, J. Phys. Chem. C. 126 (2022) 4959-4964.
[27] D. Banerjee, D. A. Popy, B. C. Leininger, T. D. Creason, V. N. Mapara, M. Furis, M. F. Borunda and B. Saparov, ACS Appl. Mater. Interfaces. 15 (2023) 30455-30468.
[28] L. Lian, P. Zhang, G. Liang, S. Wang, X. Wang, Y. Wang, X. Zhang, J. Gao, D. Zhang and L. Gao, ACS Appl. Mater. Interfaces. 13 (2021) 22749-22756.
[29] Bruker in APEX4, Vol. Bruker AXS LLC, Madison, Wisconsin, USA, 2022.
[30] Bruker in SAINT, Vol. Bruker (Ed. Bruker), Bruker AXS LLC, Madison, Wisconsin, USA, 2022, p. Bruker.
[31] L. Krause, R. Herbst-Irmer, G. M. Sheldrick and D. Stalke, J. Appl. Cryst. 48 (2015) 3-10.
[32] G. M. Sheldrick, Acta Crystallogr. 71 (2015) 3-8.
[33] G. M. Sheldrick, Cryst. Struct. Commun. 71 (2015) 3-8.
[34] O. V. Dolomanov, L. J. Bourhis, R. J. Gildea, J. A. Howard and H. Puschmann, J. Appl. Cryst. 42 (2009) 339-341.
[35] A. Spek, J. Appl. Cryst. 36 (2003) 7-13.
[36] H. Yang, S. Mandal, B. Li, T. K. Ghosh, J. M. Peterson, P. Guo, L. Dou, M. Chen and L. Huang, J. Am. Chem. Soc. 146 (2024) 33928-33936.
[37] Y. Gao, Z. Xu, L. Ye, Y. Wang and X. Zhuang, Phys. Chem. Chem. Phys. 26 (2024) 2472-2477.
[38] X. Cheng, X. Chang, Y. Lin, L. Lv, L. Cong, Y. Jia, J. Yin, J. Li and B. B. Cui, Small 20 (2024) 2307216.
[39] K. Robinson, G. Gibbs and P. Ribbe, Science 172 (1971) 567-570.
[40] Y. Li, Z. Zhou, F. K. Sheong, Z. Xing, R. Lortz, K. S. Wong, H. H. Sung, I. D. Williams and J. E. Halpert, ACS Energy Lett. 6 (2021) 4383-4389.
[41] R. P. Vasquez, Surf. Sci. Spectra. 2 (1993) 149-154.
[42] P. Cheng, L. Feng, Y. Liu, D. Zheng, Y. Sang, W. Zhao, Y. Yang, S. Yang, D. Wei

and G. Wang, Angew. Chem. Int. Ed. 59 (2020) 21414-21418.
[43] S. Ye, F. Xiao, Y. Pan, Y. Ma and Q. Zhang, Mater. Sci. Eng. R Rep. 71 (2010) 1-34.
[44] Q. Wang, H. Li, H. Tong, J. Zhu, J. Fan, S. Pan, Z. Zhou, W. Liu and G. Ouyang, Small 22 (2025) 2500660.
[45] L. Protesescu, S. Yakunin, M. I. Bodnarchuk, F. Krieg, R. Caputo, C. H. Hendon, R. X. Yang, A. Walsh and M. V. Kovalenko, Nano Lett. 15 (2015) 3692-3696.
[46] K. M. McCall, C. C. Stoumpos, S. S. Kostina, M. G. Kanatzidis and B. W. Wessels, Chem. Mater. 29 (2017) 4129-4145.
[47] M. Gerhard, B. Louis, R. Camacho, A. Merdasa, J. Li, A. Kiligaridis, A. Dobrovolsky, J. Hofkens and I. G. Scheblykin, Nat. Commun. 10 (2019) 1698.
[48] X. Hei and J. Li, Chem. Sci. 12 (2021) 3805-3817.

Graphical Abstract

We report three new lead-free copper halides with broadband STE emission, including $(OA)_4CuI_5$, which features tunable dual-band white-light emission and high color rendering, promising for solid-state lighting.